metals

MDPI

Article

Insights into the Influence of Tensile and Compressive Strain on the Microstructure and Corrosion Performance of 304 L Stainless Steel

Tongjiao Chu [1,2,*], Wenjing Xu [1] and Minghan Bai [1]

[1] Department of Material Processing Engineering, School of Materials Science and Engineering, Liaoning Technical University, Fuxin 123000, China; xwenjing0312@163.com (W.X.); aa942244410@163.com (M.B.)
[2] Shanghai Key Laboratory of Materials Laser Processing and Modification, Shanghai Jiao Tong University, Shanghai 200240, China
* Correspondence: chu_tj@163.com

Abstract: The effects of tensile and compressive strain, originating from U-bent deformation, on the corrosion behavior of 304 L stainless steel were studied via analyses of the material's microstructure and electrochemistry in a 3.5% NaCl solution. In contrast with the as-received 304 L steel with the largest grain size, the deformed 304 L material with a small grain size had the lowest number of Σ3 grain boundaries and an overall low fraction, with special low-Σ values (≤29). Moreover, the dislocation density increased to $1.13 \times 10^{16}/m^2$ and $1.4 \times 10^{16}/m^2$ for the tensile and compressive 304 L steel testing, respectively. The decrease in E_{pit} and increase in i_{pit} suggested that there was a decrease in anti-corrosion properties due to tensile and compressive deformation. This might be attributed to the higher plastic strain found in deformed 304 L steel, which can induce the rupture of passive film and have a harmful influence on corrosion resistance. In particular, the compressive 304 L steel with the highest content of deformed grains (42.12%) promoted the formation of microgalvanic cells, thereby facilitating the nucleation of pits. Then, these pits grew to a large size through grain shedding. Subsequently, massive chloride ions were generated during metal dissolution and diffused along grain boundaries, which promoted the initiation and propagation of intergranular corrosion cracks.

Keywords: compressive strain; special CSL boundaries; deformed grain; pitting; microgalvanic cells

check for updates

Citation: Chu, T.; Xu, W.; Bai, M. Insights into the Influence of Tensile and Compressive Strain on the Microstructure and Corrosion Performance of 304 L Stainless Steel. *Metals* **2024**, *14*, 1281. https://doi.org/10.3390/met14111281

Academic Editors: Andrea Di Schino and Frank Czerwinski

Received: 12 October 2024
Revised: 6 November 2024
Accepted: 6 November 2024
Published: 11 November 2024

Copyright: © 2024 by the authors. Licensee MDPI, Basel, Switzerland. This article is an open access article distributed under the terms and conditions of the Creative Commons Attribution (CC BY) license (https://creativecommons.org/licenses/by/4.0/).

1. Introduction

The product known as 304 L stainless steel is widely used industrially, e.g., in the petrochemical industry, the seawater desalination industry, and in nuclear power plants, owing to its outstanding corrosion resistance, weldability, and high strength [1,2]. During the application of 304 L steel, the deformation generated from cold working (such as shaping, rolling, bending, and drawing) may make its microstructure evolve. The strain induced by deformation weakens the pitting corrosion resistance, and sometimes even causes cracks to form around pits [3–5]. Therefore, it is important to figure out the corrosion behavior of 304 L steel under deformation conditions.

The corrosion behavior of 304 L steel under cold deformation conditions has been studied by numerous researchers. Gao et al. [6] found that a lot of deformation bands were generated with the increase in deformation, and that the pits nucleated more easily at the deformation bands in the cold-rolled austenitic stainless steel. Kishore et al. [7] suggested that a slower strain rate during prior deformation resulted in a significant decrease in the pitting corrosion resistance, whereas a higher strain rate caused an improvement when compared to an undeformed specimen. Whether prior deformation results in a detrimental or beneficial effect on corrosion resistance depends on the complicated interaction between

the crystallographic texture, dislocation density, and coincidence site lattice (CSL) boundary [7]. Luo et al. [8] reported that metastable pit initiation sites on the UNS S31803 duplex stainless steel were transformed from austenite into ferrite at a cold deformation level higher than 70%. Zakaria et al. [9] observed that pitting corrosion occurred on the outside surface of 304 L steel undergoing U-bending in a NaCl solution, which was followed by crack formation in the pit. In a study by Yoo et al. [10], the authors induced compressive stress in 304 L stainless steel through laser shock peening; it was then bent to have a U shape and its corrosion behavior was tested in a chloride solution. The results indicated that the resistance of to stress corrosion cracking by the laser-peened 304 L steel was enhanced in a chloride environment. Tsay et al. [11] revealed that the warm rolling specimen with a U-bent shape had better resistance to hydrogen embrittlement (HE) in the immersion test, while the cold rolling specimen was susceptible to sulfide stress corrosion cracking.

Compared with the tensile deformation on the outer side of the U-bent specimen, the effect of compressive deformation on the inner side of the U-bent specimen has not been assessed until now, no matter the microstructure or corrosion properties. Existing studies have presented contradictory results regarding the effect of compressive deformation on corrosion behavior. The mainstream view is that the existence of compressive strain in metal is conducive to the formation of a passive film with good protective properties [12–14]. Remarkably, Chu et al. [15] proposed that compressive stress could cause the rupture of passive films. This might enable stress corrosion cracking (SCC). However, Chu et al. [15] also pointed out that the SCC under compressive stress had a longer incubation period and a slower growth rate than under tensile stress. This suggests that the presence of tensile stress makes the occurrence of SCC under compressive stress difficult. Thus, it is exploring the effect of tensile and compressive stress on the corrosion resistance of 304 L steel is meaningful.

The major objectives of this study are to study the influences of tensile and compressive strain on the corrosion behavior of 304 L stainless steel and relate them to its microstructure. In this respect, the microstructure was comprehensively analyzed in terms of grain types, grain size, grain boundary types, crystal plane orientation, and dislocation at different deformation conditions by combining the scanning electron microscopy (SEM) and electron back-scatter diffraction (EBSD) techniques. The effect of bending deformation on corrosion behavior was then explored by electrochemical corrosion tests. By further considering the results of corrosion tests, the relationship between microstructure and corrosion behavior was analyzed. This study is expected to broaden our understanding of the corrosion mechanism of 304 L stainless steel under tensile and compressive deformation conditions.

2. Materials and Methods

2.1. Materials and Deformation Method

We utilized 304 L stainless steel (Baosteel, Shanghai, China) in this study. Its chemical composition is as follows (in wt.%): 0.025C, 18.09Cr, 8.08Ni, 0.34Si, 1.390Mn, 0.032P, 0.030S, and balance Fe. Different plastic strains can be obtained through bending deformation. Firstly, the 304 L sheet was cut to the dimensions of 75 mm × 25 mm × 2 mm, as shown in Figure 1a. And then two types of U-bent specimens were prepared through the three-point-bend loading method. The U1 specimen was analyzed with a focus on the tensile stress on the outside of the U-bent specimen (Figure 1b). The U2 specimen was analyzed with a focus on the compressive stress existing on the inner side of the U-bent specimen (Figure 1c). The following formula can be used to approximately calculate the strain level (ε) at the exposed area [16]:

$$\varepsilon = t/2R \quad (1)$$

where t and R, respectively, represent the specimen thickness and the radius of curvature at the area of interest. Thus, the tensile strain and compressive strain were 8% and 10%, respectively. In this way, the differences in microstructure and corrosion behavior between tensile and compressive deformation could be evaluated. After deformation, all specimens were subjected to annealing at 1050 °C for 5 min.

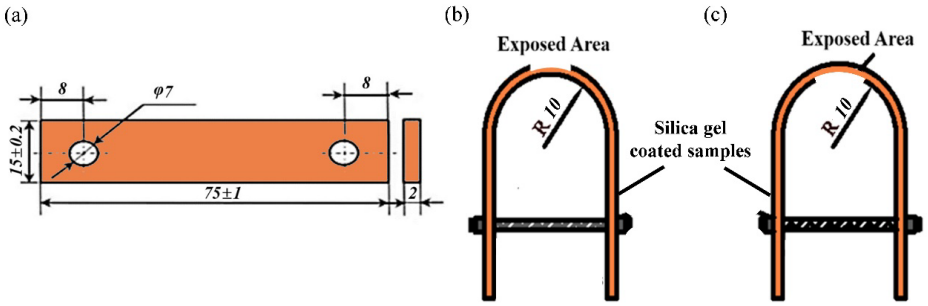


Figure 1. Preparation schematic of U-bending sample: (**a**) schematic diagram of 304 L sheet; (**b**) U-bending sample named U1 under tensile deformation; (**c**) U-bending sample named U2 under compressive deformation.

2.2. Electrochemical Measurements

SiC paper with 180–2000 grit was used to sequentially ground the U-bent specimens. This was followed by rinsing with deionized water and alcohol, and then drying. The specimen was connected by a copper wire. The deformed area of 1 cm^2 remained the exposure area used for electrochemical measurements. And the other areas were sealed with silica gel. A conventional three-electrode cell system was used to conduct electrochemical measurements in the workstation (PARSTAT4000, Princeton Applied Research, Oak Ridge, TN, USA). The reference electrode and counter electrode were, respectively, a saturated calomel electrode (SCE) and a platinum sheet. The specimens were the working electrodes. The aggressive Cl^- can take on the roles of damaging the passive film and causing the pit initiation. Therefore, the 3.5% NaCl solution was selected as the corrosion medium to evaluate the corrosion resistance of materials in order to guarantee the safe operation of nuclear power structures in extreme environments. Before the tests, all specimens were exposed to the 3.5% NaCl solution for 30 min to stabilize the open current potential. Then, we performed the measurement of potentiodynamic anodic polarization and electrochemical impedance spectroscopy (EIS, PARSTAT4000, Princeton Applied Research, Oak Ridge, TN, USA) was adopted. The potentiodynamic polarization tests were conducted in the range of −0.2 V to 1.5 V, with a scanning rate of 0.5 mV/s. The EIS was measured in the frequency range from 10 kHz to 0.01 Hz by superimposing an AC voltage with a 10 mV amplitude.

2.3. Microstructure Characterization

The microstructures of the deformed specimens were examined using SEM (SUPRA40, Carl Zeiss AG, Oberkochen, Germany). This was paired with EDS for elemental analysis (Ultim Max 65, Oxford Instruments, Oxford, UK). Electron backscatter diffraction (EBSD, HKL Nordlys, Oxford Instruments, Oxford, UK) was performed using FEG SEM (Mira 4, Tescan, Brno, Czech Republic), employing the EBSD detector for microstructural characterization via the extraction of grain information and recrystallization information. The step size used during EBSD testing was 0.5 μm.

3. Results

3.1. Characterization of Microstructure

3.1.1. Analysis of Morphology and Grain Type

The SEM images shown in Figure 2 further confirmed that there was an austenite microstructure before and after deformation. The grains in the as-received 304 L sample were freely distributed, and the twins within the grain were obvious, as displayed in Figure 2a. Parallel slip lines were distinctively identified for the deformed samples because of the lower stacking fault energy in the austenite phase [8], indicating that the tensile and compressive strain produced a high dislocation density [17], as specified in the magnification of Figure 2d,f. Tiny precipitates were observed in some grains without slip lines in the deformed samples.

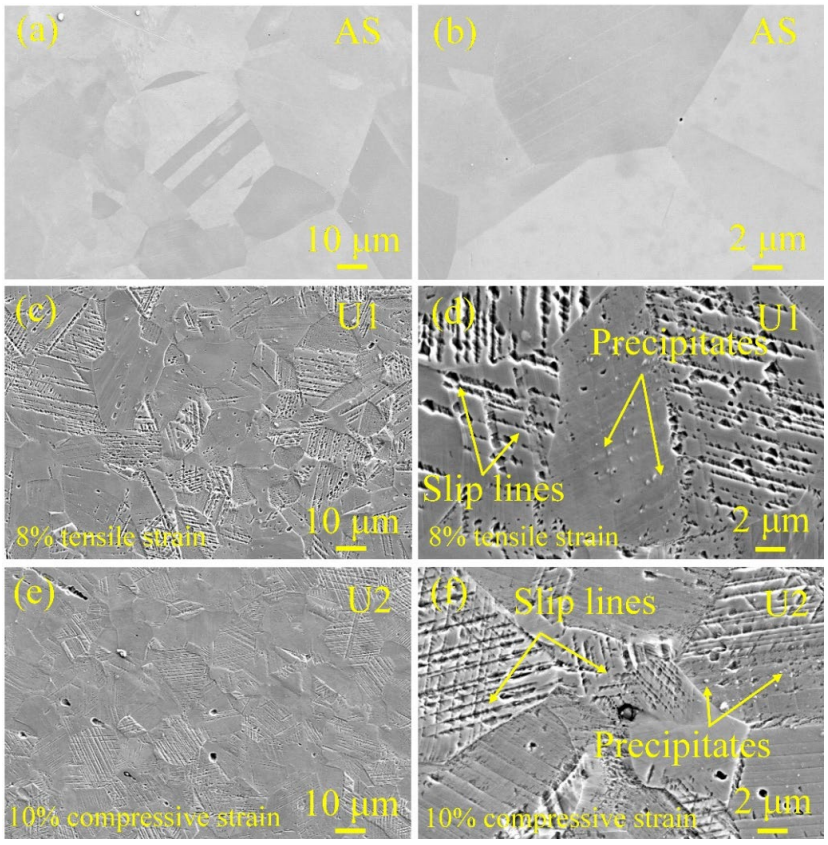


Figure 2. SEM microstructure of specimens under different deformation conditions: (**a**,**b**) AS sample (AS is short for as-received 304 L); (**c**,**d**) U1 sample with 8% tensile strain; (**e**,**f**) U2 sample with 10% compressive strain; (**b**,**d**,**f**) sample with high magnification, corresponding to (**a**–**c**).

We found that the grain size decreased obviously after deformation. The grain size distribution for specimens under various conditions is displayed in Figure 3. The distribution range of grain sizes in Figure 3a was wide for the AS sample. The as-received 304 L steel had the largest grain size of 70 μm, and its average grain size was around 64.39 μm. The distribution of grain size was narrow for deformed samples. For the U1 specimen with 8% tensile strain and the U2 specimen with 10% compressive strain, the average grain size decreased to 13.44 μm and 12.74 μm, respectively. Generally, the grain size decreased after bending, which was possibly related to the dynamic recrystallization [18]. Grain refinement caused the grain boundary density to increase, which can strengthen the mechanical properties but weaken corrosion resistance to some extent.

Furthermore, the grain types in different specimens are displayed in Figure 4 and their fractions were computed further. In the absence of deformation, the austenite mainly consisted of recrystallized grains. Compared with the as-received 304 L steel, the U1 and U2 samples had fewer recrystallized grains and more substructured and deformed grains. The formation of substructured grains was ascribed to the large residual stress and the heat treatment process. The U1 sample with 8% tensile strain mainly consisted of substructured grains. The U2 sample with 10% compressive strain had the highest fraction of deformed grains, indicating the large deformation induced during the bending process. The heterogeneity in the recrystallized fractions of samples under different deformation conditions might affect their corrosion performance.

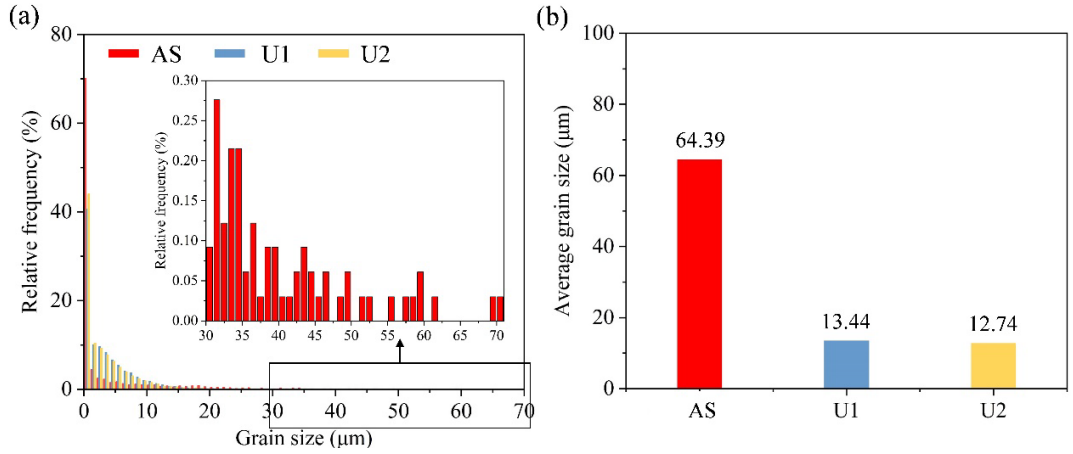


Figure 3. Grain size information under different deformation conditions: (**a**) grain size distribution; (**b**) average grain size.

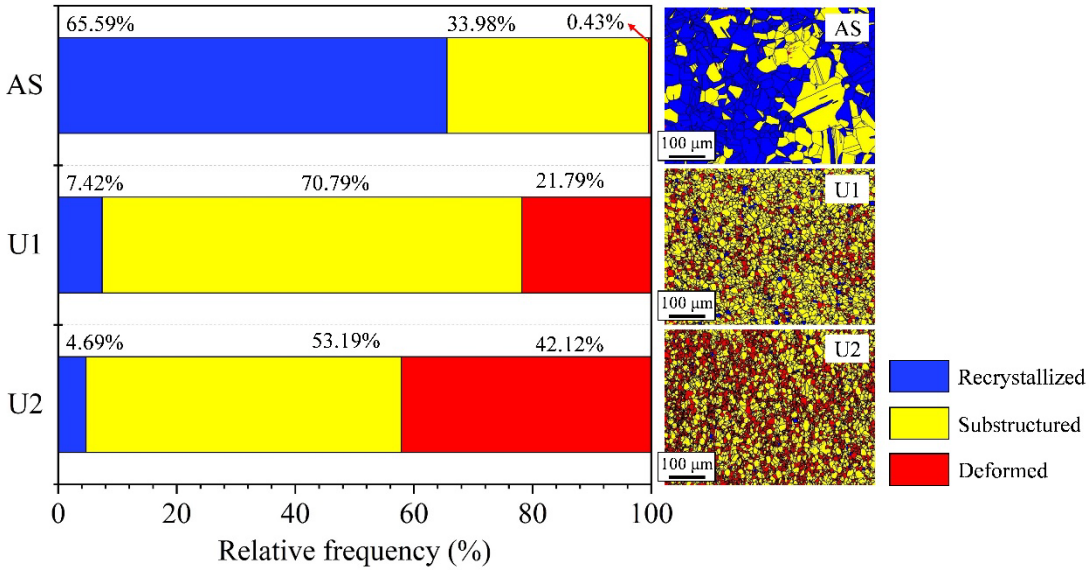


Figure 4. The distributions and relative frequencies of grain types under different deformation conditions: recrystallized grains, substructured grains, and deformed grains are shown in blue, yellow, and red, respectively. The red arrow points out the frequency of deformed grains in AS samples.

3.1.2. Grain Boundary Characteristics

According to lots of studies on grain boundaries, the crystallographic structure of the grain boundaries might control grain boundary diffusion, cracking, and corrosion [19]. When compared with high-energy boundaries, low-energy grain boundaries are highly resistant to the deterioration of grain boundaries [20]. Figure 5 displays the distribution of grain boundaries for samples with different deformation conditions. The low-Σ values ($\leq$29) in the CSL framework are regarded as special grain boundaries, and they exhibit good resistance to segregation, sliding, corrosion, and SCC when contrasted to the high-Σ CSL boundaries (>29) and other high-angle grain boundaries. The low-Σ values ($\leq$29) in the CSL framework can be divided into Σ3 CSL, (Σ9 + Σ27) CSL, and other low CSL values. It is shown in Figure 5a that the Σ3 CSL grain boundaries were higher and straighter in the as-received 304 L steel. A few (Σ9 + Σ27) CSL boundaries appeared among the Σ3 CSL grain boundaries. Figure 6a demonstrates that the fraction of Σ3 CSL boundaries was around 53.26%. A high fraction of CSL boundaries made the random boundaries discontinuous, causing the alleviation of grain boundary deterioration. Furthermore, the

CSL boundaries with low interfacial energy can also improve the corrosion performance of materials. The Σ3 CSL boundaries were still large in U1 and U2 samples (Figure 5c,e). They were dense but short and tortuous. The fractions of Σ3 CSL boundaries for the U1 sample with 8% tensile strain and the U2 sample with 10% compressive strain were, respectively, 14.36% and 10.96%, which were lower than those of the as-received 304 L steel. Meanwhile, Figure 6a indicated that the as-received 304 L steel had the highest fraction of special CSL boundaries (≤Σ29). The decrease in CSL boundaries during the pre-strain process might damage the corrosion resistance of deformed 304 L steel.

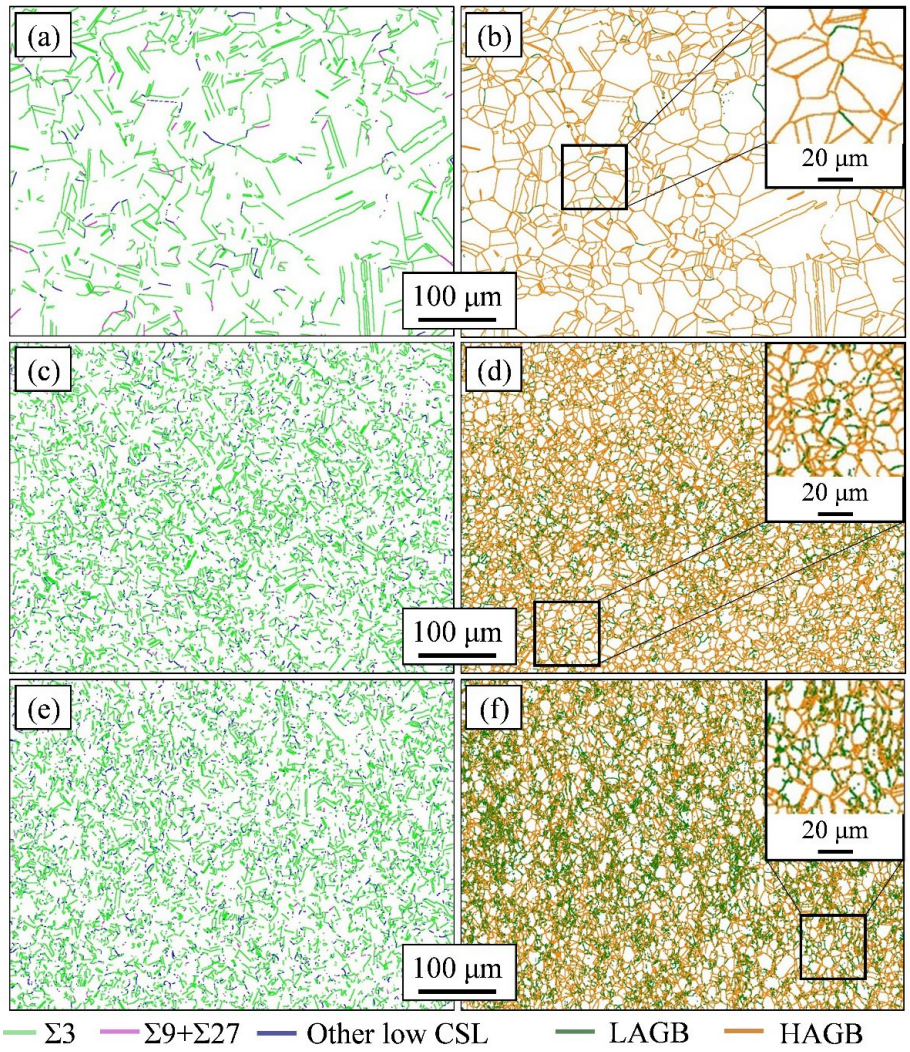


Figure 5. Grain boundary types of 304 L steel under different deformation conditions: (**a**,**c**,**e**) the distribution of special CSL boundaries (≤Σ29)—the Σ3 boundaries are shown by light green lines, the Σ9 + Σ27 boundaries are shown by pink lines, and other low CSL boundaries are shown by blue lines; (**b**,**d**,**f**) the distribution of HAGB (yellow lines) and LAGB (dark green lines). (**a**,**b**) The as-received 304 L steel, (**c**,**d**) the U1 sample with 8% tensile strain, and (**e**,**f**) the U2 sample with 10% compressive strain.

Ordinarily, low-angle grain boundaries (LAGBs) and high-angle grain boundaries (HAGBs) compose the grain boundaries in 304 L steel. Taking the different interfacial energies into account, their contents are important to the corrosion performance. The misorientation angles of LAGB and HAGB were, respectively, defined as smaller than 2° and larger than 15° in this work. Figure 5b indicated that the HAGBs were the major grain boundary type for the sample without deformation, and a few LAGBs were located

inside the austenite. The fraction of various grain boundaries was determined according to the grain boundary distribution, as exhibited in Figure 6b. It could be seen that the as-received 304 L only had a proportion of 8% for LAGBs. Grain boundary density increased significantly for the deformed samples, as displayed in Figure 5d,f. These were consistent with the decrease in grain size mentioned above. Similarly to the AS sample, the LAGBs were also located inside the fine austenite. The LAGBs in the deformed samples increased significantly, especially for the U2 sample with 10% compressive strain. Figure 6b indicated that the percentages of LAGBs were 68% for the U2 sample and 60% for the U1 sample. The decrease in HAGB and the decrease in HAGB suggested that the grain nucleation and growth occurred through the migration of random high-angle grain boundaries and the generation of LAGB boundaries.

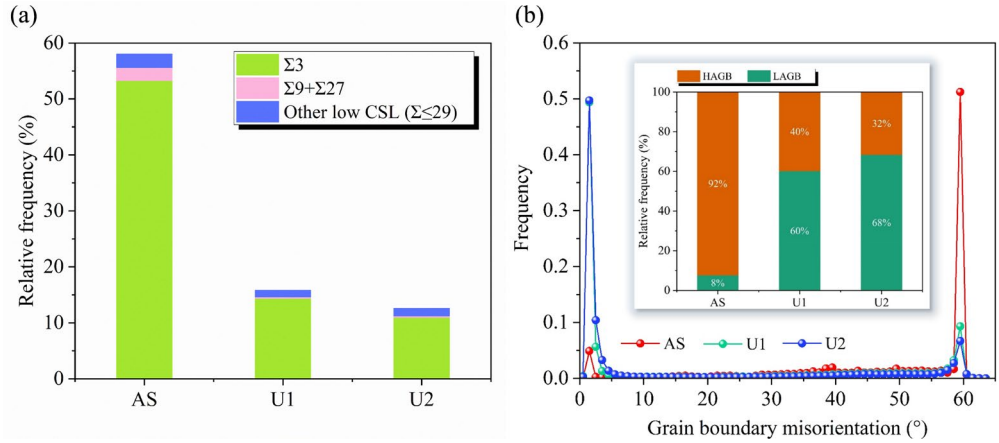


Figure 6. The fraction of the special grain boundaries of 304 L steel under different deformation conditions: (**a**) special CSL boundaries (≤Σ29); (**b**) HAGBs and LAGBs.

3.1.3. Evolution of Crystal Plane Orientation

The presence of different crystal plane orientations in metals can result in different properties [21]. The {100}, {110}, and {111} crystal planes were commonly used to study the properties of 304 L steel. Inverse pole figure (IPF) subset maps of specimens are provided in Figure 7, displaying the distribution of specific crystal plane orientations at different deformation conditions. The crystal plane orientation preferences in all samples were different.

The main crystal plane orientation in the as-received 304 L steel was {100}, which accounted for 11.2%. While the U1 samples and U2 samples displayed different features, they had a higher fraction of {110} crystal plane than {100} crystal plane. The basis directions <001>, <101>, and <111> can be used to predict the corrosion rate when considering the orientation. Similarly, {001} < {101} < {111} was the order of corrosion rates when considering the grain [22,23]. The grains adjacent to the {001} planes have the highest corrosion resistance [24,25]. Continuous dissolution implies the occurrence of corrosion. The surface metal is oxidized at the beginning and then dissolves. These processes will eliminate the surface layer and cause the exposure of underlying planes. It was evident that the <100> direction was the main orientation in the as-received 304 L steel, while the U1 sample with 8% tensile strain and the U2 sample with 10% compressive strain were orientated towards the <110> direction. These parameters caused the lowest corrosion rate for the AS sample and the highest for deformed samples.

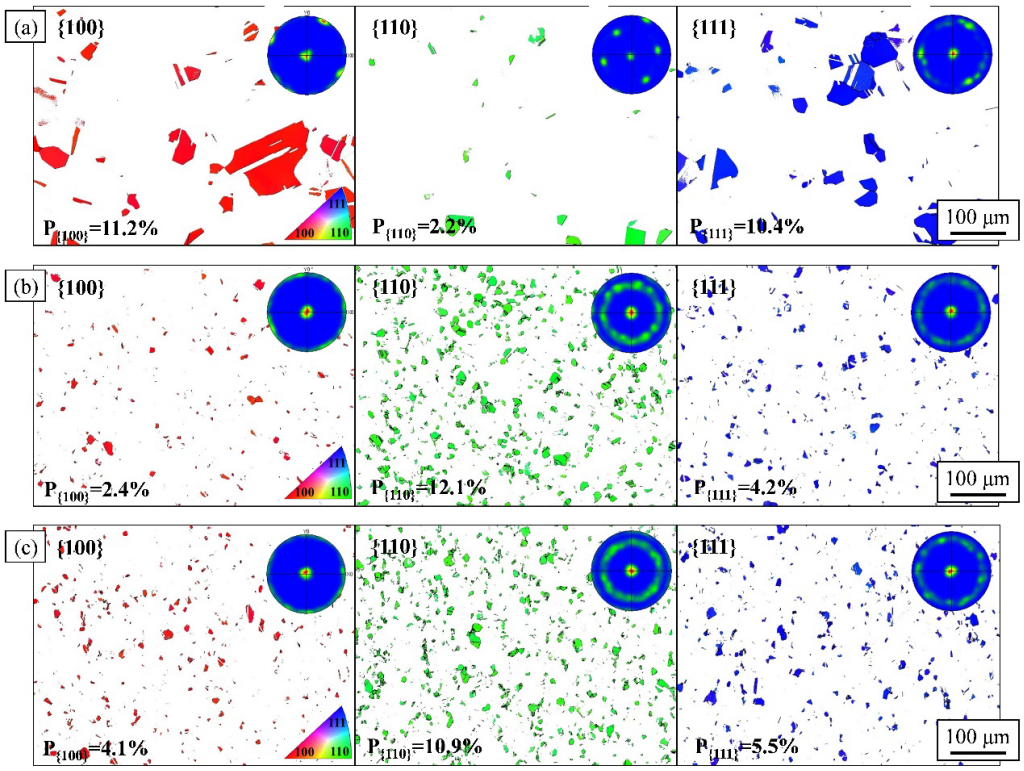


Figure 7. The distribution of specific crystal plane orientations under different deformation conditions: (**a**) the as-received 304 L steel; (**b**) the U1 sample with 8% tensile strain; (**c**) the U2 sample with 10% compressive strain. P{100}, P{110}, and P{111} represent the content of {100}, {110} and {111} crystal planes.

3.1.4. Dislocation Density Evolution

Figure 8 displays the local misorientation (LMO) analysis results of the 304 L steel under different deformation conditions. The LMO degree increased from 1° for as-received 304 L steel up to 2° on the U1 sample, and rose to 3° on the U2 sample, respectively. The increase in the LMO degree suggested that large plastic strains existed in the specimens suffering deformation. For the U2 sample with a 10% compressive strain, the LMO presented a broader distribution, as shown in Figure 8f, indicating intensified strain and a high density of dislocations [26].

The kernel average misorientation (KAM) method [27] can be used to settle the local misorientation and further quantitatively study the dislocation density in specimens with different deformation conditions. The extra geometrically necessary dislocations (GNDs) accumulated during the deformation were associated with strain level. Therefore, the mean GND was used to analyze the relationship between the basal slip and the ratcheting effect during the bending process. The following formula, devised according to the strain gradient theory, was the simple method used to calculate the GND density information [28]:

$$\rho^{\mathrm{GND}} = \frac{2\Delta\theta_{\mathrm{i}}}{\mu b} \tag{2}$$

where ρ^{GND} is the GND density, $\Delta\theta_{\mathrm{i}}$ represents the local misorientation, μ is the step size used during EBSD testing, and b is the Burgers vector. The calculated GND density under different deformation conditions is given in Figure 8. It was found that the dislocation density of the U2 sample with 10% compressive strain was significantly higher than the densities of the others.

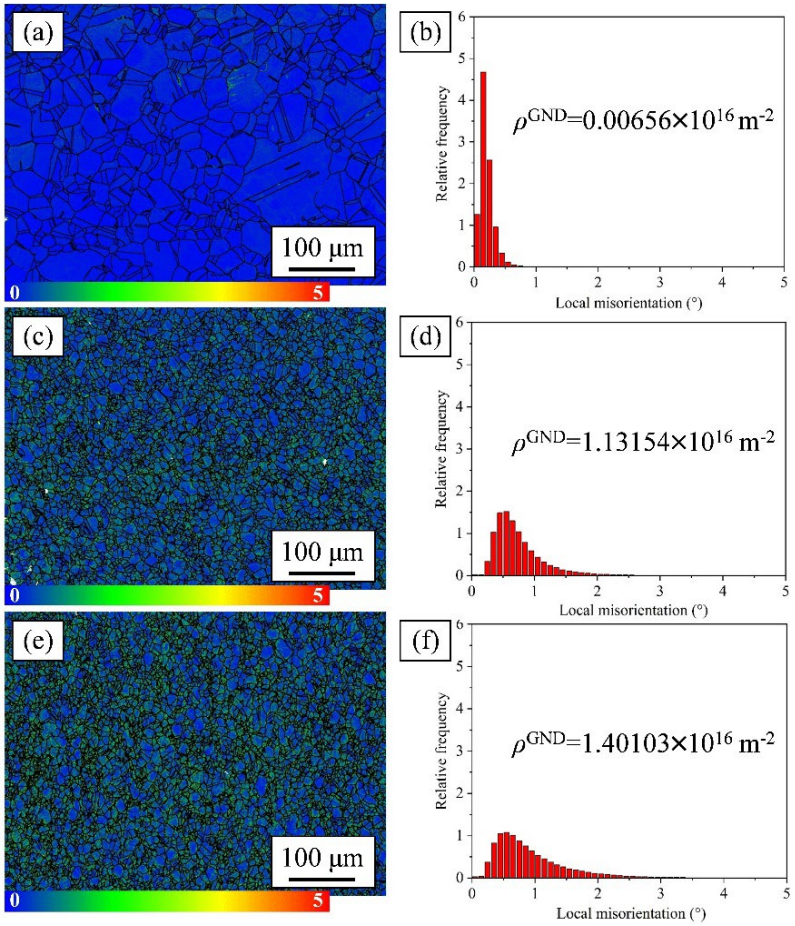


Figure 8. EBSD local misorientation maps: (**a**,**b**) the as-received 304 L steel; (**c**,**d**) the U1 sample with 8% tensile strain; (**e**,**f**) the U2 sample with 10% compressive strain. (**b**,**d**,**f**) The calculated mean GND densities.

3.2. Effect of Bending Deformation on Corrosion Behavior

3.2.1. Potentiodynamic Polarization Results

The potentiodynamic polarization curves of samples under different deformation conditions are exhibited in Figure 9. The Tafel fitting method was used to obtain the corrosion potential. Table 1 displays the electrochemical parameters for different specimens. All specimens had roughly the same corrosion potential (E_{corr}). However, the current densities (i_{corr}) of the U1 sample and the U2 sample were 1.77 μA·cm^{-2} and 3.23 μA·cm^{-2}, respectively. The U2 achieved the highest i_{corr}, corresponding to the lowest i_{corr} of the as-received 304 L steel (0.21 μA·cm^{-2}). The relatively high i_{corr} indicated that the U2 had weak corrosion resistance.

Table 1. Electrochemical parameters of the potentiodynamic polarization.

Specimen	i_{corr} (μA·cm^{-2})	E_{corr} (V)	E_{pit} (V)	i_p (μA·cm^{-2})
As-received 304 L	0.21	−0.37	0.53	0.09
U1	1.77	−0.31	-	-
U2	3.23	−0.39	−0.07	1.48

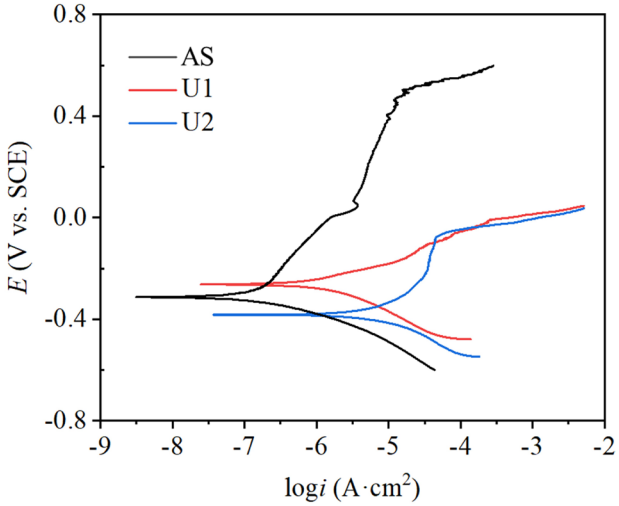


Figure 9. Potentiodynamic polarization results of 304 L steel under different deformation conditions in a 3.5 wt.% NaCl solution.

The passivation region can be at the inflection point where the slope of the potentiodynamic polarization curve changes significantly [29]. The average current density in this region was calculated as the passivation current density (i_p). The potential at which the current density exceeded 50 μA/cm^2 was regarded as the breakdown potential (E_{pit}) [30]. The E_{pit} reflected the rupture of the passivation film [31,32]. The as-received 304 L steel had the highest E_{pit} (0.53 V), suggesting the best resistance to pitting. The U2 sample had the lowest E_{pit} (−0.07 V), and the U1 sample exhibited no obvious passivation characteristics. Meanwhile, it was observed that the i_p at the U2 sample was mildly higher than that of the as-received 304 L steel. Therefore, potentiodynamic polarization results indicated that introducing strain, especially for the U2 sample, weakened the corrosion resistance of 304 L steel. The deterioration of the anti-corrosion properties of the U2 sample with 10% compressive strain might be closely associated with dislocation multiplication, the decline in Σ3 CSL, and incremental change in surface energy. The dissolution rate of the passivation film can be reflected by the value of i_p [33,34]. As displayed in Figure 4, the presence of lots of substructured and deformed grains in U1 and U2 implied the existence of high residual stress. Thus, the passive film was more easily destroyed, causing the deterioration of corrosion resistance.

3.2.2. Electrochemical Impedance Spectroscopy Results

The passivation of 304 L steel under different deformation conditions was analyzed through the EIS. The Nyquist curve (Figure 10a), going from high frequency to low frequency, demonstrated that the regular semicircular capacitive arc existed in all the samples. The capacitive arc radius for the as-received 304 L steel was larger than that of the samples with bending deformation. The EIS data were fitted through the equivalent circuits. The model of $R_s(Q_1\ R_{ct})$ was adopted for the as-received 304 L steel, and $R_s(Q_1\ (R_f(Q_2\ R_{ct})))$ was adopted for U1 and U2. R_s, R_f, and R_{ct} were solution resistance, passive film resistance, and charge transfer resistance, respectively. The non-ideal capacitance (constant phase element—CPE) caused by the heterogeneous current flow was denoted by Q_1. And Q_2 represented constant capacitance of the interface double layer. Figure 10d and Table 2 display the main fitting results. It was found that the variable $Y_0(Q_1)$ of the as-received 304 L steel was the lowest, and that of the U2 sample was the largest. The R_{ct} value was considered to reflect the anti-corrosion properties of the metal. The U1 and U2 samples under strain conditions had similar but small R_{ct} values, which were 2325 Ω·cm^2 and 2081Ω·cm^2, respectively. The R_{ct} for the as-received 304 L was the largest (244,600 Ω·cm^2). Deformation in 304 L steel allowed the charges generated from anodic dissolution transfer much more easily. The R_f values of U1 and U2 were 4454 Ω·cm^2 and 1551 Ω·cm^2, respectively. This meant that the

passive film in the U2 sample with 10% compressive strain had slightly weaker protective properties than the U1 sample with 8% tensile strain. These results were consistent with the i_p results obtained in potentiodynamic polarization tests.

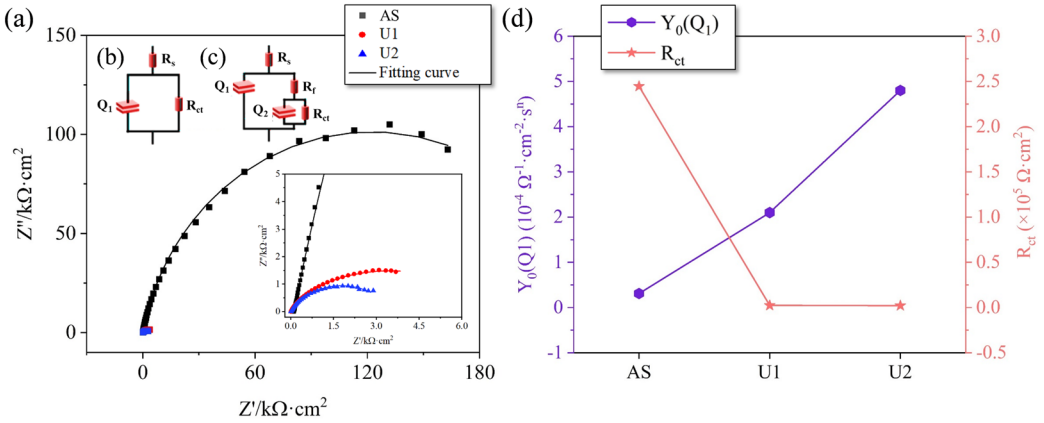


Figure 10. EIS results of samples under different deformation conditions in 3.5 wt.% NaCl solution: (**a**) Nyquist plots; (**b**,**c**) equivalent circuit models; (**d**) Y_0 (Q_1) and R_{ct}.

Table 2. Equivalent circuit parameters for impedance spectra.

Fitting Parameters	As-Received 304 L	U1	U2
R_s ($\Omega \cdot cm^2$)	110.3	7.427	2.678
R_{ct} ($\Omega \cdot cm^2$)	2.446×10^5	2.325×10^3	2.081×10^3
Q_1 ($\Omega^{-1} \cdot cm^{-2} \cdot s^n$)	3.1×10^{-5}	2.1×10^{-4}	4.8×10^{-4}
Q_2 ($\Omega^{-1} \cdot cm^{-2} \cdot s^n$)	-	3.93×10^{-4}	8.73×10^{-4}
$\sum c^2$	6.14×10^{-4}	3.30×10^{-4}	3.19×10^{-4}

3.2.3. Microstructural Features After Corrosion

Figure 11 displays the corrosion morphologies of samples, obtained via electrochemical tests, under different deformation conditions. Without bending deformation, the pits were small and few. These pits were in the shape of hemispheres, as shown in Figure 11a. Obviously, the matrix of as-received 304 L steel was free from intergranular corrosion. The size and number of pits in U1 were significantly larger than those in the as-received 304 L steel, suggesting that it had worse resistance to pitting. This observation matched well with the results of E_{pit} and i_p. Dissimilarly, the pits were irregular for the U2 sample with 10% compressive strain, as displayed in Figure 11e. It can be seen in Figure 11f that the austenite grain shedding resulted in the formation of the large pit. Nearby it, the grain boundaries were eroded clearly. The eroded grain boundaries indicated that the intergranular corrosion was fairly continuous. Meanwhile, there were small pits distributed inside grains. The large pit, emerging due to grain shedding or continuous corrosion along grain boundaries, was evidence of serious pitting on the U2 sample.

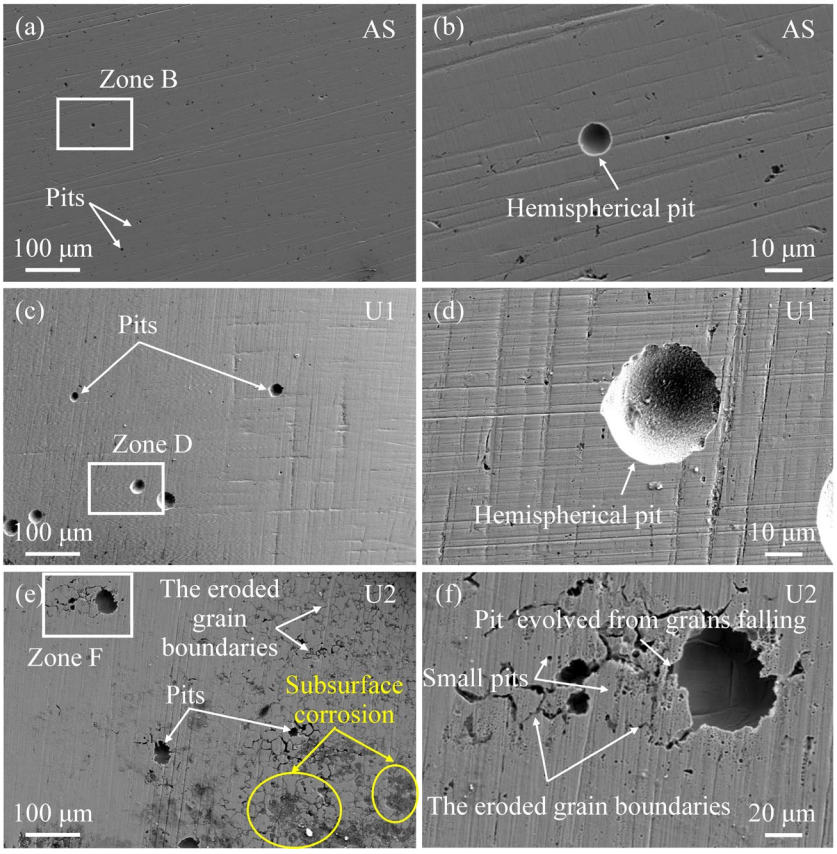


Figure 11. Corrosion morphologies on the surface of samples under different deformation conditions: (**a**,**b**) as-received 304 L steel; (**c**,**d**) U1 sample; (**e**,**f**) U2 sample. (**b**,**d**,**f**) High magnification corresponding to (**a**–**c**).

4. Discussion

The aforementioned results revealed that strain featuring both tension and compression made the pitting sensitivity increase. When no strain was present in 304 L steel, no obvious dislocation existed in the austenite. In this situation, the relatively lower pitting resistance equivalent number (PREN) of austenite and the high energy of the grain boundary might be responsible for the occurrence of pitting corrosion [35]. When we added bending deformation to 304 L, dislocation movement was able to occur in the form of slip bands (Figure 2d,f). Given that the higher dislocation density existed in U1 and U2 samples (Figure 8d,f), more available sites can be activated for pit initiation. Concurrently, the decline in Σ3 CSL (Figure 6b) also weakened anti-corrosion properties in grain boundaries [36]. Due to the above reasons, the U1 sample with 8% tensile strain and the U2 sample with 10% compressive strain had larger-sized pits and higher numbers of pits.

In addition, the recrystallization level in the U2 sample was lower due to it having the highest strain. This resulted in lots of deformed grains still existing when compared with the U1 sample. This directly contributed to the differences in corrosion behaviors between the U1 and U2 samples, as shown schematically in Figure 12. The largest fraction of deformed grains in the U2 sample, acting as active sites, were susceptible to being corroded preferentially. As exhibited in Figure 12d, the deformed grain and recrystallized grain can form microgalvanic cells in a 3.5% NaCl solution, thereby accelerating metal dissolution and facilitating the nucleation of pits in the deformed grain. The microgalvanic cells might be among the key factors leading to the nucleation of pits in the U2 sample, and then these pits grew in the mode of grain shedding. In particular, the deformed grains were adjacent to each other. When they dissolved and dropped together, a large pit formed. Beyond that, high concentrations of Cl^- ions were generated during metal dissolution.

These Cl^- ions diffused along grain boundaries, accelerating corrosion at grain boundaries. Furthermore, due to stress concentrations, the plastic strain on the pit bottom and shoulder evolved to be much higher with the increase in pit depth and diameter, which promoted the initiation of cracking. Thus, the intergranular corrosion cracks formed near pits, as shown in Figure 12e. In contrast, the process of metal dissolution behaved relatively mildly for the U1 sample with a lower fraction of deformed grains. Thus, the pit might nucleate at some sites with HAGBs or other defects. Without the role of microgalvanic cells, the pit cannot grow to a large size and have little effect on the surrounding microstructure, as displayed in Figure 12b,d.

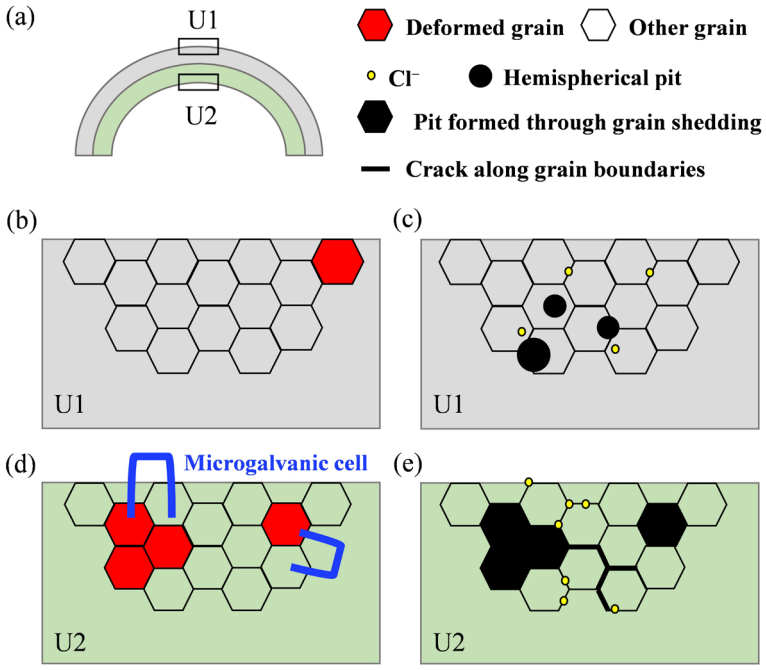


Figure 12. Schematic diagrams demonstrating the relationship between microstructure and corrosion behavior of samples in different deformation conditions: (**a**) U-bending specimen showing the location of U1 and U2 samples; (**b**,**c**) U1 sample with 8% tensile strain; (**d**,**e**) U2 sample with 10% compressive strain.

The present study indicated the U-bent samples had more severe corrosion than the as-received sample, and the corrosion rate could be accelerated by both tensile and compressive strain. In addition, compressive strain had a more obvious influence than tensile strain. This might be ascribed to the massive metal dissolution seen at higher strain levels. A lot of research has reported that the metal dissolution rate significantly rises when plastic strain increases. The plastic strain mainly promotes metal anodic activity. Gutman et al. [37] built a model to describe the mechanoelectrochemical effect using the abundant studies in thermodynamics. The anodic dissolution resulting from plastic strain can be determined using the following kinetic equation:

$$\frac{i}{i_n} = \left(\frac{\Delta\varepsilon}{\varepsilon_0} + 1\right) exp\frac{\sigma_m V_m}{RT} \tag{3}$$

where i and i_n are anodic currents with deformation and without deformation, respectively. $\Delta\varepsilon$ and ε_0 are the plastic strain and the onset of strain hardening. σ_m is the spherical part of the macroscopic stress tensor, relying on the applied load. V_m, R, and T are molar volume, gas constant, and temperature. The i/i_n is the mechano-electrochemical influence factor. Based on the Gutman model, the distribution of local strains can change the local anodic dissolution rate. The higher plastic strain, suggesting a higher i/i_n, could result in the

breakdown of the passive film and weaken its anti-corrosion properties. That was the reason for the pit nucleation and growth under the compressive strain for the U2 sample.

The corrosion behavior of 304 L steel could be influenced by strain at a certain point. This agrees with the microstructure evolution. The findings in this study can offer a theoretical basis for the use of the deformed 304 L steel in usual situations. In other severe conditions, the corrosion performance of deformed 304 L steel might undergo some changes. This needs to be further explored in a subsequent study to advance the application range of the deformed 304 L steel.

5. Conclusions

The effects of tensile and compressive strain on the corrosion performance of 304 L steel were studied in 3.5% NaCl solution through microstructural analyses and electrochemical tests. The following main conclusions can be drawn from the present work:

1. In contrast with the as-received 304 L steel with the largest grain size, the U2 sample with 10% compressive strain and the smallest grain size had the lowest Σ3 values and an overall low fraction of special low-Σ values ($\leq$29). Similarly, the special low-Σ values ($\leq$29) were few for the U1 sample with 8% tensile strain.
2. The decrease in E_{pit} and increase in i_p suggested the deterioration of anti-corrosion properties by U-bent deformation. Compared with the as-received 304 L steel with the main orientation of <100> direction, the U1 and U2 orientating towards <110> were more prone to pitting. This also showed that the compressive deformation allowed the pit to initiate and grow more than tensile deformation.
3. The highest content of deformed grains (42.12%) in the U2 sample promoted the formation of microgalvanic cells and the nucleation of pits in the deformed grain, and then these pits grew to large sizes through grain shedding. In addition, massive Cl^- ions generated during metal dissolution diffused along grain boundaries, which promoted the initiation and propagation of intergranular corrosion cracks.
4. Due to the strain originating from U bending, the dislocation density increased to $1.13 \times 10^{16}/m^2$ for the U1 sample and to $1.4 \times 10^{16}/m^2$ for the U2 sample. The local strain distributions caused differences in the local anodic dissolution rate. A higher plastic strain in the U2 sample, suggesting the higher i/i_n, could cause the breakdown of the passive film and have a detrimental role on corrosion resistance.

Author Contributions: Conceptualization, T.C. and W.X.; methodology, T.C. and W.X.; validation, T.C.; formal analysis, T.C.; investigation, T.C. and M.B.; writing—original draft preparation, T.C. and W.X.; writing—review and editing, T.C., W.X., and M.B.; supervision, W.X. and M.B. All authors have read and agreed to the published version of the manuscript.

Funding: The project was supported by Open Fund of Shanghai Key Laboratory of Materials Laser Processing and Modification (No. 20-1133). The authors gratefully acknowledge the Discipline Innovation Team of Liaoning Technical University (No. LNTU20TD-16).

Data Availability Statement: The original contributions presented in the study are included in the article material, further inquiries can be directed to the corresponding author.

Conflicts of Interest: The authors declare no conflicts of interest.

References

1. Lee, W.S.; Lin, C.F. Impact properties and microstructure evolution of 304L stainless steel. *Mat. Sci. Eng. A* **2001**, *308*, 124–135. [CrossRef]
2. Acharyya, S.G.; Khandelwal, A.; Kain, V.; Kumar, A.; Samajdar, I. Surface working of 304L stainless steel: Impact on microstructure, electrochemical behavior and SCC resistance. *Mater. Charact.* **2001**, *72*, 68–76. [CrossRef]
3. Al-Duheisat, S.A.; El-Amoush, A.S. Effect of deformation conditions on the corrosion behavior of the low alloy structural steel girders. *Mater. Des.* **2016**, *89*, 342–347. [CrossRef]
4. Renton, N.C.; Elhoud, A.M.; Deans, W.F. Effect of plastic deformation on the corrosion behavior of a super-duplex stainless steel. *J. Mater. Eng. Perform.* **2011**, *20*, 436–444. [CrossRef]

5. Peguet, L.; Malki, B.; Baroux, B. Influence of cold working on the pitting corrosion resistance of stainless steels. *Corros. Sci.* **2007**, *49*, 1933–1948. [CrossRef]
6. Gao, Z.H.; Wang, R.J.; Li, J.X.; Xu, L.N.; Qiao, L.J. Effect of cold rolling on the pitting corrosion of 316L and 304 austenitic stainless steels. *J. Mater. Sci.* **2022**, *57*, 20503–20520. [CrossRef]
7. Kishore, K.; Chandan, A.K.; Sahoo, B.K.; Meena, L.K. Novel observation of dominant role of strain rate over strain during pre-straining on corrosion behaviour of 304L austenitic stain-less steel. *Mater. Chem. Phys.* **2022**, *277*, 125522. [CrossRef]
8. Luo, H.; Wang, X.; Dong, C.; Xiao, K.; Li, X. Effect of cold deformation on the corrosion behaviour of UNSS31803 duplex stainless steel in simulated concrete pore solution. *Corros. Sci.* **2017**, *124*, 178–192. [CrossRef]
9. Zakaria, W.N.L.W.; Kee, K.E.; Ismail, M.C. The effect of sensitization treatment on chloride induced stress corrosion cracking of 304L stainless steel using U-bend test. *Mater. Today Proc.* **2020**, *29*, 75–81. [CrossRef]
10. Yoo, Y.R.; Choi, S.H.; Kim, Y.S. Effect of laser shock peening on the stress corrosion cracking of 304L stainless steel. *Metals* **2023**, *13*, 516–537. [CrossRef]
11. Tsay, L.W.; Lin, Y.J.; Chen, C. The effects of rolling temperature and sensitization treatment on the sulfide stress corrosion cracking of 304L stainless steel. *Corros. Sci.* **2012**, *63*, 267–274. [CrossRef]
12. Yang, Q.; Luo, J.L. Effects of hydrogen and tensile stress on the breakdown of passive films on type 304 stainless steel. *Electrochim. Acta* **2002**, *46*, 851–859. [CrossRef]
13. Qin, Z.; Li, X.; Xia, D.H.; Zhang, Y.; Wu, Z.; Hu, W. The effect of compressive stress on cavitation-erosion corrosion behavior of 304 stainless steel. *Anti-Corros. Method. Mater.* **2022**, *69*, 434–441. [CrossRef]
14. Lu, J.Z.; Luo, K.Y.; Yang, D.K.; Cheng, X.N.; Hu, J.L.; Dai, F.Z.; Qi, H.; Zhang, L.; Zhong, J.S.; Wang, Q.W. Effects of laser peening on stress corrosion cracking (SCC) of ANSI304 austenitic stainless steel. *Corros. Sci.* **2012**, *60*, 145–152. [CrossRef]
15. Chu, W.Y.; Yao, J.; Hsiao, C.M. Stress corrosion cracking of austenitic stainless steel under compressive stress. *Corros. Sci.* **1984**, *40*, 302–306. [CrossRef]
16. Li, M.C.; Cheng, Y.F. Corrosion of the stressed pipe steel in carbonate-bicarbonate solution studied by scanning localized electrochemical impedance spectroscopy. *Electrochim. Acta* **2008**, *53*, 2831–2836. [CrossRef]
17. Gutierrez-Urrutia, I.; Raabe, D. Dislocation and twin substructure evolution during strain hardening of an Fe-22 wt.% Mn-0.6 wt.% C TWIP steel observed by electron channeling contrast imaging. *Acta Mater.* **2011**, *59*, 6449–6462. [CrossRef]
18. Cao, F.; Jiang, T.; Hou, W.; Huang, G.; Shen, Y.; Ding, Y.; Shu, P. Effect of inhomogeneous fiber structure on the mechanical properties of friction stir welded SAF 2507 super duplex stainless steel. *Mater. Chem. Phys.* **2022**, *283*, 126026. [CrossRef]
19. Michiuchi, M.; Kokawa, H.; Wang, Z.J.; Sato, Y.S.; Sakai, K. Twin-induced grain boundary engineering for 316 austenitic stainless steel. *Acta Mater.* **2006**, *54*, 5179–5184. [CrossRef]
20. Lehockey, E.M.; Brennenstuhl, A.M.; Thompson, I. On the relationship between grain boundary connectivity, coincident site lattice boundaries, and intergranular stress corrosion cracking. *Corros. Sci.* **2004**, *46*, 2383–2404. [CrossRef]
21. Wang, B.; Xin, R.; Huang, G.; Liu, Q. Effect of crystal orientation on the mechanical proper-ties and strain hardening behavior of magnesium alloy AZ31 during uniaxial compression. *Mat. Sci. Eng. A* **2012**, *534*, 588–593. [CrossRef]
22. Dong, S.; Chen, X.; La Plantea, E.C.; Gussev, M.; Leonard, K.; Sant, G. Elucidating the grain-orientation dependent corrosion rates of austenitic stainless steels. *Mater. Des.* **2020**, *191*, 108583. [CrossRef]
23. Wang, P.; Zhao, J.; Ma, L.; Cheng, X.; Li, X. Effect of grain ultra-refinement on microstructure, tensile property, and corrosion behavior of low alloy steel. *Mater. Charact.* **2021**, *179*, 111385. [CrossRef]
24. Hu, S.; Mao, Y.; Liu, X.; Han, E.; Hannienn, H. Intergranular corrosion behavior of low-chromium ferritic stainless steel without Cr-carbide precipitation after aging. *Corros. Sci.* **2020**, *166*, 108420. [CrossRef]
25. Tokita, S.; Kokawa, H.; Sato, S.Y.; Fujii, H.T. In situ EBSD observation of grain boundary character distribution evolution during thermomechanical process used for grain boundary engineering of 304 austenitic stainless steel. *Mater. Charact.* **2017**, *131*, 31–38. [CrossRef]
26. Fukuoka, C.; Morishima, K.; Yoshizawa, H.; Mino, K. Misorientation development in grains of tensile strained and crept 2.25% Cr-1% Mo steel. *Scr. Mater.* **2002**, *1*, 61–66. [CrossRef]
27. Calcagnottok, M.; Ponge, D.; Demir, E.; Raabe, D. Orientation gradients and geometrically necessary dislocations in ultrafine grained dual phase steels studied by 2D and 3D EBSD. *Mater. Sci. Eng. A* **2010**, *527*, 2738–2746. [CrossRef]
28. Yan, Z.; Wang, D.; He, X.; Wang, W.; Zhang, H.; Dong, P.; Li, C.; Li, Y.; Zhou, J.; Zhuang, L. De-formation behaviors and cyclic strength assessment of AZ31b magnesium alloy based on steady ratcheting effect. *Mat. Sci. Eng. A* **2018**, *723*, 212–220. [CrossRef]
29. Bellezze, T.; Giuliani, G.; Roventi, G. Study of stainless steels corrosion in a strong acid mixture. Part 1: Cyclic potentiodynamic polarization curves examined by means of an analytical method. *Corros. Sci* **2018**, *130*, 113–125. [CrossRef]
30. Macdonald, D.D.; Heaney, D.F. Effect of variable intensity ultraviolet radiation on passivity breakdown of AISI type 304 stainless steel. *Corros. Sci* **2000**, *42*, 1779–1799. [CrossRef]
31. Li, W.; Li, J.; Gu, J.; Zhang, Q. Correlation between hyperfine structure of inclusion and localized corrosion mechanism of DSS2101 with Ce microalloying in simulated marine environment. *Vacuum* **2021**, *191*, 110361. [CrossRef]
32. Salehi, M.; Yeganeh, M.; Heidari, R.B.; Eskandari, M. Comparison of the microstructure, cor-rosion resistance, and hardness of 321 and 310S austenitic stainless steels after thermo-mechanical processing. *Mater. Today Commun.* **2022**, *31*, 103638. [CrossRef]
33. Fu, Y.; Wu, X.; Han, E.; Ke, W.; Yang, K.; Jiang, Z. Effects of cold work and sensitization treatment on the corrosion resistance of high nitrogen stainless steel in chloride solutions. *Electrochim. Acta* **2009**, *54*, 1618–1629. [CrossRef]

34. Heine, B.; Kirchheim, R. Dissolution rates of iron and chromium and Fe-Cr alloys in the passive state. *Corros. Sci.* **1990**, *31*, 533–538. [CrossRef]
35. Tan, H.; Jiang, Y.; Deng, B.; Sun, T.; Xu, J.; Li, J. Effect of annealing temperature on the pitting corrosion resistance of super duplex stainless steel UNS S32750. *Mater. Charact.* **2009**, *60*, 1049–1054. [CrossRef]
36. Han, L.; Han, T.; Chen, G.; Wang, B.; Sun, J.; Wang, Y. Influence of heat input on microstruc-ture, hardness and pitting corrosion of weld metal in duplex stainless steel welded by key-hole-TIG. *Mater. Charact.* **2021**, *175*, 111052. [CrossRef]
37. Gutman, E.M. *Mechanochemistry of Materials*, 1st ed.; Cambridge International Science Publishing: Cambridge, UK, 1998; pp. 122–146.

Disclaimer/Publisher's Note: The statements, opinions and data contained in all publications are solely those of the individual author(s) and contributor(s) and not of MDPI and/or the editor(s). MDPI and/or the editor(s) disclaim responsibility for any injury to people or property resulting from any ideas, methods, instructions or products referred to in the content.